Facile Synthesis and Enhanced Ultraviolet Emission of ZnO Nanorods Prepared by Vapor-Confined Face-to-Face Annealing

Giwoong Nam,[†] Youngbin Park,[†] Iksoo Ji,[†] Byunggu Kim,[†] Sang-heon Lee,[‡] Do Yeob Kim,[§] Soaram Kim,[§] Sung-O Kim,[§] and Jae-Young Leem*,[†]

[†]Department of Nanoscience & Engineering, Inje University, 197, Inje-ro, Gimhae-si, Gyeongsangnam-do 621-749, Republic of Korea
[‡]School of Chemical Engineering, Yeungnam University, Gyengsan 712-749, Republic of Korea
[§]Holcombe Department of Electrical and Computer Engineering, Center for Optical Materials Science and Engineering Technologies (COMSET), Clemson University, Clemson, South Carolina 29634, United States

Ⓢ Supporting Information

ABSTRACT: In this study, we report a novel regrowth method of sol–gel-prepared ZnO films using a vapor-confined face-to-face annealing (VC-FTFA) technique in which mica was inserted between two films, followed by annealing with the FTFA method. The ZnO nanorods are regrown when zinc acetate dihydrate and zinc chloride ($ZnCl_2$) are used as the solvent, because these generate $ZnCl_2$ vapor. The near-band-edge emission intensity of the ZnO nanorods was enhanced through the VC-FTFA method, increasing significantly by a factor of 56 compared to that of ZnO films annealed in open air at 700 °C. Our method may provide a route toward the facile fabrication of ZnO nanorods.

KEYWORDS: *zinc oxide, zinc chloride, regrowth, photoluminescence, spin-coating method*
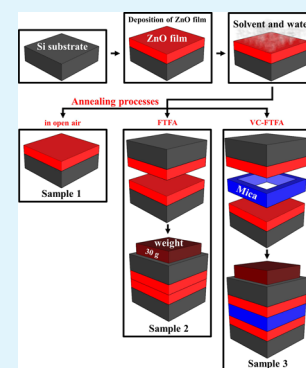
1. INTRODUCTION

One-dimensional (1D) nanostructures, including nanorods, nanowires, and nanotubes, have aroused considerable research interest in numerous areas of nanoscience and nanotechnology. There are two reasons for this interest: first, 1D nanostructures have unusual and unique physical properties, such as quantum-mechanical confinement effects (QCEs)[1−4] and second, they have a high surface-to-volume ratio, making them important for the development of new devices and sensors.[5−7] In particular, it is believed that QCEs play a crucial role in improving the optical properties of materials.[8,9] ZnO exhibits a direct bandgap of 3.37 eV, a high exciton binding energy of 60 meV (which is considerably larger than that of GaN (25 meV)), and a favorable thermal energy at room temperature (RT, ∼26 meV), which act together to ensure an efficient exciton emission under ambient conditions. A broad range of potential high-performance applications are based on 1D ZnO nanomaterials, such as the field of UV lasers, photodetectors, field-effect transistors, solar cells, chemical sensors, superhydrophobic surfaces, and nanogenerators.[10−16] Considerable efforts have been devoted to the synthesis of 1D ZnO nanostructures, and various approaches have been demonstrated for the fabrication of semiconducting ZnO nanowires or nanorods. There are numerous techniques for the preparation of ZnO nanorods, such as a metal−organic chemical vapor deposition, chemical vapor deposition, the hydrothermal method, electrochemical deposition, and chemical bath deposition.[17−21] Another option

is the sol−gel spin-coating method, which is conventionally used for thin film deposition, but not an ideal method for the growth of 1D nanostructures. If this method could be adapted to the growth of nanorods, it would provide advantages such as reproducibility, low cost, and mass production capability.

A face-to-face annealing (FTFA) approach is frequently employed for GaAs semiconductors to prevent the out-diffusion of arsenic.[22] The GaAs wafer to be annealed is placed between a bottom Si wafer and a top GaAs wafer with the polished surfaces facing one another, which is why this approach is called FTFA. In this study, we used a sol−gel spin-coating technique combined with a novel annealing method, the vapor-confined FTFA (VC-FTFA), to fabricate ZnO nanorods, using zinc chloride to regrow them. The VC-FTFA method has several advantages over conventional FTFA methods, including a sharp increase in the near-band-edge (NBE) emission intensity of the photoluminescence (PL) spectra. In this study, we describe the mechanism for the vapor generation during annealing and the influence of the confined vapors during the VC-FTFA on the optical properties of the ZnO nanorods.

2. EXPERIMENTAL METHODS

Preparation of ZnO Films. The precursor solutions for the ZnO films were prepared by dissolving zinc acetate dihydrate (Zn-$(CH_3COO)_2\cdot2H_2O$, ACS Reagent, >98%, Sigma-Aldrich) and zinc chloride ($ZnCl_2$, >98%, Guaranteed Reagent, Junsei Chemical Co. Ltd.) in 2-methoxyethanol (99.8%, Sigma-Aldrich). The concentration of the metal precursors was 0.5 M. Monoethanolamine (C_2H_7NO, MEA, ACS Reagent, >99.0%, Sigma-Aldrich) was used as a stabilizing agent to improve the solubility of the precursor salt. The molar ratio of MEA to the metal salts was 1.0 (1.204 mL), and the ratio of the Zn in zinc chloride ($Zn_{chloride}$) to that in the zinc acetate dihydrate ($Zn_{acetate}$) was fixed at 1.5 atom %. The masses of the zinc acetate dihydrate and zinc chloride were 4.324 and 0.041 g, respectively. The volume of the precursor solution was 40 mL. The stabilized sol−gel solution was stirred at 60 °C for 2 h until it became clear and homogeneous, and then it was subsequently cooled to RT and aged for 24 h before being used as the coating solution to deposit the films. The p-type (<0.005 $\Omega\cdot$cm) Si (100) substrates (18 mm × 18 mm) were ultrasonically cleaned in acetone for 10 min, followed by a second 10 min cleaning in ethanol, rinsed with deionized water, and blow-dried with nitrogen. The precursor solution was then spin-coated onto a p-Si substrate at 2000 rpm for 20 s, followed by drying the films at 200 °C for 10 min in an oven. These spin-coating and drying procedures were repeated five times.

Fabrication of ZnO Nanorods though Regrowth. The basic strategy for annealing spin-coated ZnO films ($Zn_{chloride}/Zn_{acetate}$ = 1.5 atom %) is illustrated in Figure 1. Three samples were prepared at 700 °C in a furnace (WiseTherm, FP-05) for a comparative study. Sample 1 was annealed in open air. Sample 2 was annealed using the conventional FTFA method, in which two films were placed together in an FTF arrangement during annealing. For sample 3, mica was inserted between the two films, and these were then annealed using
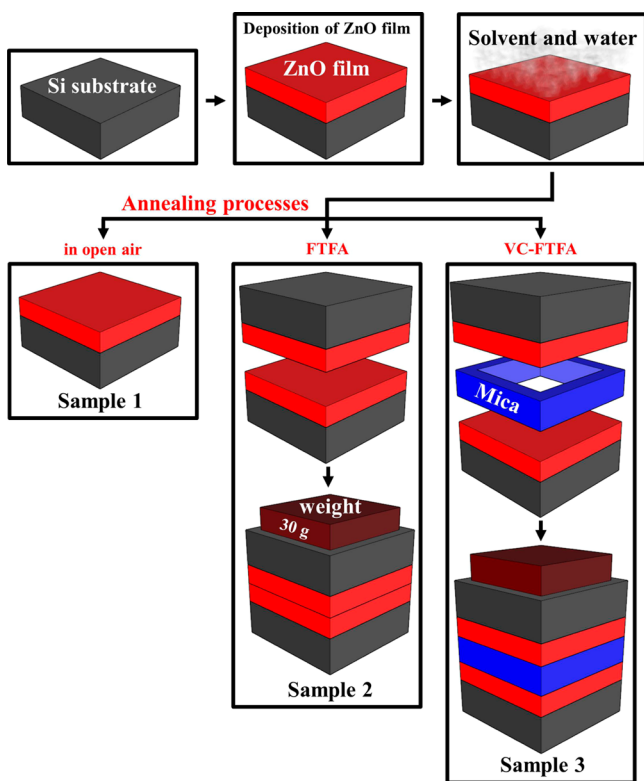
the FTFA method. During the annealing process, we put a counterpoise (30 g) on samples 2 and 3 to confine any vapors.

Characterization. The PL properties of the ZnO nanorods were investigated via PL measurements using a He−Cd laser (325 nm) with a 20 mW excitation power and a 0.75 m single grating monochromator with a photomultiplier tube (HAMAMATSU, R928) using the photocount method at 12 and 300 K. The surface morphology was analyzed using a field-emission scanning electron microscope (FE-SEM, HITACHI, S-4800). The thermal analyses of the zinc acetate dihydrate and zinc chloride/zinc acetate dihydrate precursors were performed using a thermogravimetry-differential thermal analyzer (TG-DTA, TA Instruments, SDT Q600) at a heating rate of 10 °C/min in air. To fabricate the electrodes, In and Al metals were deposited onto the ZnO nanorods and p-Si substrate, respectively, via thermal evaporation. The current−voltage characteristics of the devices were measured by applying a direct current voltage to the device using a source meter (Keithley, 2400).

3. RESULTS AND DISCUSSION

The thermal-decomposition behaviors of the zinc acetate dihydrate ($Zn_{chloride}/Zn_{acetate}$ = 0 atom %, precursor 1) and zinc chloride/zinc acetate dihydrate ($Zn_{chloride}/Zn_{acetate}$ = 1.5 atom %, precursor 2) precursors were determined using a TG-DTA to understand their thermal stability and decomposition temperature; precursors 1 and 2 were heated in the TG-DTA from RT to 600 °C at a constant rate of 10 °C/min in air as shown in Figure 2. The TG-DTA curves revealed that precursors 1 and 2 exhibited an initial weight loss of 5.5 and 5.6%, respectively, in the temperature region of 27−150 °C, which resulted from the thermal dehydration of the zinc acetate dihydrate. Precursor 1 became anhydrous zinc acetate. Further decomposition of the anhydrous zinc acetate caused a weight loss near 150 °C, and the decomposition process was completed before 300 °C was reached, accompanying an exothermic reaction. A 60.9% weight loss was greater than the calculated theoretical weight loss of 46.5%. The extra 14.4% weight loss can be attributed to the sublimation of the zinc acetate species or the formation of other volatile zinc organic compound such as $Zn_4O(CH_3COO)_6$.[23,24] Therefore, as the temperature increased, precursor 1 gradually decomposed to form ZnO through the following chemical reactions:[24]

$$Zn(CH_3COO)_2\cdot2H_2O \rightarrow Zn(CH_3COO)_2 + 2H_2O(\uparrow) \tag{1}$$

$$4Zn(CH_3COO)_2 + 2H_2O$$
$$\rightarrow Zn_4O(CH_3COO)_6 + 2CH_3COOH(\uparrow) \tag{2}$$

$$Zn_4O(CH_3COO)_6 + 3H_2O \rightarrow 4ZnO + 6CH_3COOH(\uparrow) \tag{3}$$

$$Zn_4O(CH_3COO)_6$$
$$\rightarrow 4ZnO + 3CH_3COCH_3(\uparrow) + 3CO_2(\uparrow) \tag{4}$$

In comparison, precursor 2 exhibited weight losses in the temperature regions of 150−200 and 200−300 °C, which were attributed to the decomposition of organic compounds and then generated CH_3COOH and HCl vapors. Specifically, in the temperature region of 300−600 °C, precursor 2 slowly evaporated, generating $ZnCl_2$ vapor, as described by the following reactions:

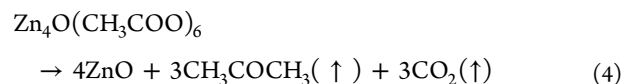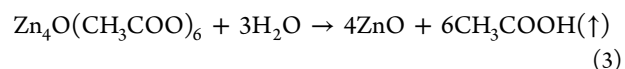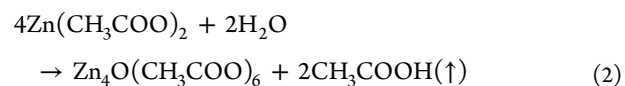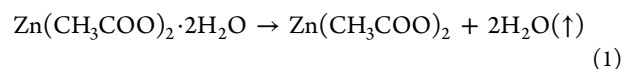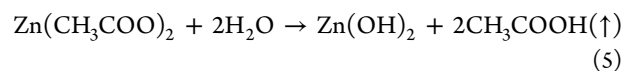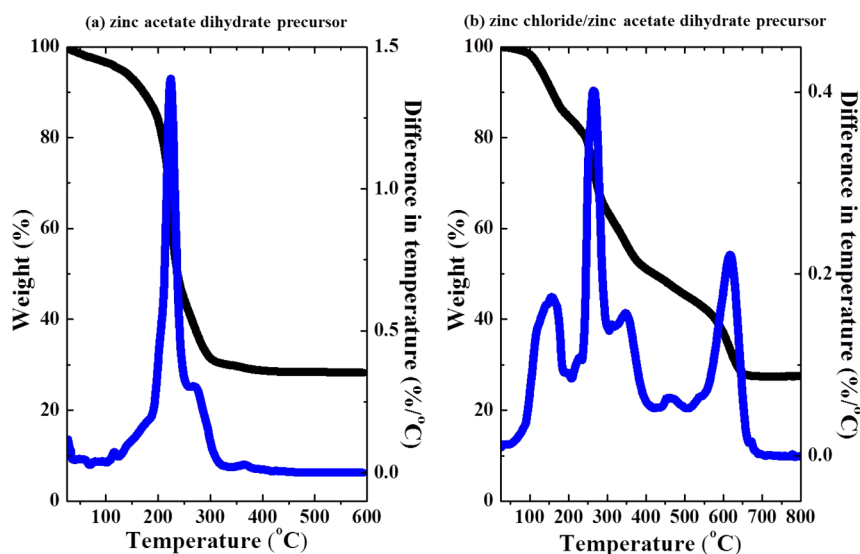$$Zn(CH_3COO)_2 + 2H_2O \rightarrow Zn(OH)_2 + 2CH_3COOH(\uparrow) \tag{5}$$

Figure 1. Schematics of the ZnO nanorod fabrication process. The annealing configurations: annealing of a single film without any additional film (sample 1) or the FTFA with an additional film (sample 2). In the schematic diagram of sample 2, mica was inserted between the two films (sample 3).
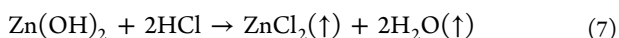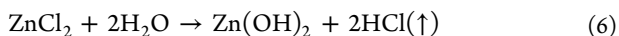
Figure 2. TGA and DTA curves for the (a) zinc acetate dihydrate and (b) zinc chloride/zinc acetate dihydrate precursors, shown as the percentage of weight loss (black lines) and the difference in temperature (blue lines).
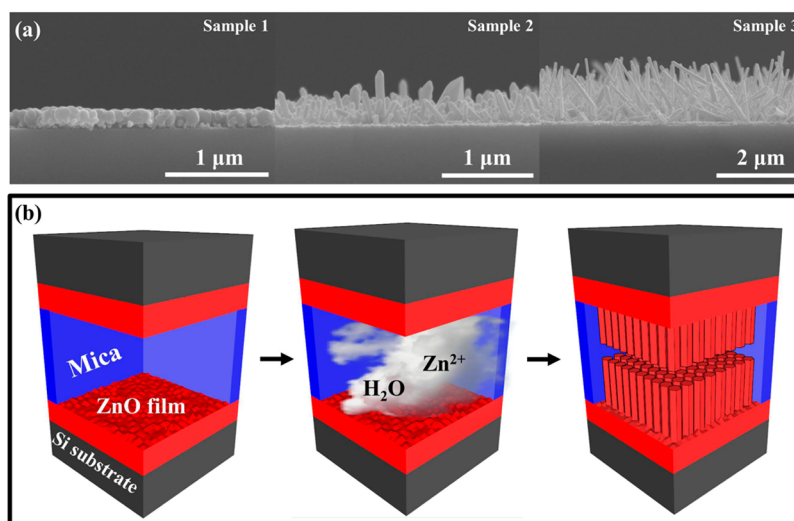

Figure 3. (a) SEM images of the three samples. (b) Schematics of the ZnO nanorod regrowth mechanism for sample 3.

$$ZnCl_2 + 2H_2O \rightarrow Zn(OH)_2 + 2HCl(\uparrow) \tag{6}$$

$$Zn(OH)_2 + 2HCl \rightarrow ZnCl_2(\uparrow) + 2H_2O(\uparrow) \tag{7}$$

Both precursor 1 and 2 presented endothermic and exothermic peaks between 25 and 330 °C and between 25 and 550 °C, respectively, in the heat flow analysis; these peaks were attributed to the evaporation of water and organics from these precursors. The final exothermic peaks in the TG-DTA curves of precursors 1 and 2, at 370 and 580 °C, respectively, resulted from the crystallization of the ZnO.

Sample 1, which was annealed in open air, consisted of numerous round ZnO particles of approximately 100 nm in diameter, as shown in the FE-SEM image presented in Figure 3a. Prior to the annealing treatment, there were numerous dangling bonds at the grain boundaries related to oxygen vacancies. These grains merged into adjacent particles to form larger particles (approximately 100 nm in diameter) during the annealing process in open air. The ZnO nanorods were then grown using the FTFA and VC-FTFA methods, using the round ZnO nanoparticles as a seed layer for the nanorod

growth. The $ZnCl_2$ vapor was generated in the temperature region of 300−600 °C, and the round nanoparticles were regrown by this $ZnCl_2$ vapor. Sample 2, which utilized two ZnO films facing one another in the FTFA method, was then compared with sample 3, which underwent the same method but with a mica between them. The mica was used for sample 3 to confine the generated $ZnCl_2$ vapor. The length of the nanorods in sample 3 was greater than the length of those in sample 2 because the vapor was confined by the mica. The growth of the ZnO nanorods can be attributed to the vapor−solid mechanism, in which nanorods grow via the oxidation of produced Zn vapor, followed by condensation, as shown in Figure 3b. The $ZnCl_2$ vapors decomposed between 400−600 °C, and the Zn vapors absorbed on the round nanoparticles with oxygen-containing organic compounds. In contrast, the surface morphology of the ZnO films did not change after annealing treatment when they were prepared using a precursor of only zinc acetate dihydrate (Figure S1, Supporting Information). According to the chemical reactions shown in eqs 1−4, an acetate-based solvent cannot generate vapors that
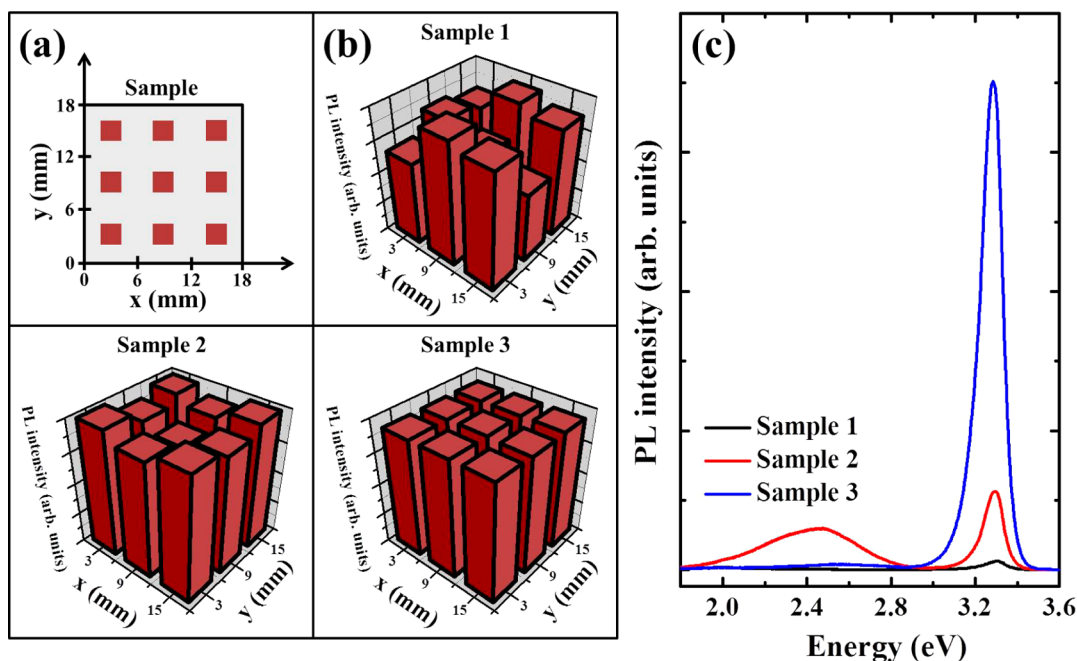
Figure 4. (a) Samples were measured at the marked brown squares to show NBE emission intensity uniformity. (b) The degree of NBE emission intensity uniformity in the PL spectra of the three samples. (c) PL spectra of the three samples at 300 K.

facilitate the regrowth; thus, when using a chloride-based solvent the ZnO nanorods formed by regrowth because it generated $ZnCl_2$ vapor.

We obtained the degree of NBE emission intensity uniformity in the PL spectra for the three samples (Figure 4b) using a continuous-wave helium−cadmium (He−Cd) laser as the optical excitation source, and these intensities were measured at the points marked in red in Figure 4a. The NBE emission intensities were randomly distributed across the entire surface of sample 1, whereas those of sample 2 were stronger near the edges of the sample surface than toward its center, due to the generated $ZnCl_2$ vapor not being sufficiently confined. This vapor only remained briefly at the surface center, slightly regrowing the round nanoparticles. However, for sample 3, the NBE emission intensities appeared to be evenly distributed over the entire surface because the vapor was confined by the mica. We attributed the active regrowth seen in sample 3 to the confinement of this vapor. Figure 4c presents the PL spectra of the three samples. All three samples exhibited an NBE peak at 3.283 eV, attributed to the ZnO phase. The NBE emission intensity was clearly enhanced by VC-FTFA method, increased by a factor of 56 compared to that of films annealed in open air. The spectra of all three samples also contain a green emission band at approximately 2.460 eV originating from the recombination of holes with the electrons occupying singly ionized oxygen vacancies.[25] The ZnO nanorod regrowth resulting from the VC-FTFA method is effective in increasing not only the NBE emission intensity but also the emission uniformity. In contrast, the NBE emission intensity of a ZnO film annealed in open air produced using a zinc acetate dihydrate precursor was similar to that of an identical film annealed using the VC-FTFA method (Figure S2, Supporting Information). However, the yellow-orange emission band of the ZnO films annealed using the VC-FTFA method was slightly less than that of the ZnO films annealed in open air. This result is similar to that reported by Wang et al.,[26] and it is not attributable to regrowth. Chloride-containing metals, such as

magnesium chloride ($MgCl_2$), can generate $ZnCl_2$ and other metal chloride vapors, which were found to increase the NBE emission intensity and create a blue shift of the NBE emission peaks (Figure S3, Supporting Information).

Figure 5 presents the PL spectra of ZnO films annealed using the VC-FTFA method with various annealing temperatures
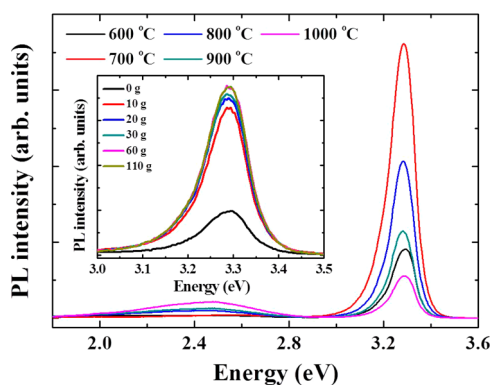
Figure 5. PL spectra of the ZnO nanorods produced using the VC-FTFA method at different temperatures. (inset) The PL spectra of the ZnO nanorods produced using the VC-FTFA method with various weights at 700 °C.

(600−1000 °C). As the annealing temperature was increased to 700 °C, the NBE emission intensity also increased. The NBE emission intensity of the film annealed at 600 °C was the lowest because the $ZnCl_2$ vapor was only minimally generated and decomposed. At an annealing temperature of 700 °C, the $ZnCl_2$ vapor was fully generated and decomposed, with the resultant vapor remaining between the ZnO films to cause active regrowth. Conversely, the NBE emission intensity decreased as the annealing temperature was increased to 1000 °C, because the $ZnCl_2$ vapor activated by this thermal energy was not well-confined, escaping from the region between the ZnO films. Therefore, length and density of ZnO nanorods were increased

with increasing annealing temperature up to 700 °C and were decreased in more than 700 °C (Figure S4, Supporting Information). However, at an annealing temperature of 1000 °C, ZnO film was not regrown because all ZnCl$_2$ vapors were escaped from the region between the ZnO films. During the VC-FTFA process at 700 °C, we put various weights (0, 10, 20, 30, 60, and 110 g) on the ZnO films to confine the ZnCl$_2$ vapor. The NBE emission intensity of the ZnO nanorods increased when the weight was increased to 30 g but was smiliar to masses above 30 g, as shown in the inset of Figure 5. Therefore, to confine the ZnCl$_2$ vapor, the weight needs to be at least 30 g.

Figure 6 shows the PL spectra of samples 1 and 3 measured at 12 K. Four distinct PL peaks appeared in the spectra of
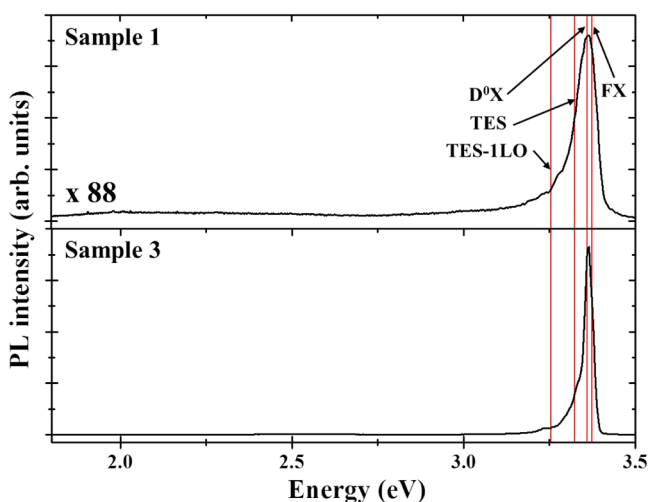

Figure 6. PL spectra at 12 K of samples 1 and 3.

samples 1 and 3 at 3.376, 3.361, 3.323, and 3.251 eV. The NBE emission peaks at 3.376, 3.361, and 3.323 eV were attributed to the emission of free excitons (FX), neutral donor-bound excitons (D^{0}X), and two-electron satellites (TES), respectively.[27] The peak at 3.251 eV was attributed to the first-order longitudinal optical phonon replicas of TES (TES-1LO). It is known that the LO phonon replicas of TES in ZnO have usually been identified based on the energy interval between a TES and the LO phonon energy ($h\omega_{LO}$ = 72 meV).[28] In general, a TES is another characteristic of the D^{0}X transition in the spectral region of 3.32−3.34 eV.[27] Bound excitons are extrinsic transitions related to dopants or defects, which usually create discrete electronic states in the bandgap. In theory, excitons could be bound to neutral or charged donors and acceptors. The shallow neutral donor-bound exciton often dominates due to the presence of donors from unintentional impurities and/or shallow donor-like defects. During the recombination of a D^{0}X, the final state of the donor can be a 1s (the normal D$_i^0$X line) or a 2s/2p state (the TES$_i$ line). The energy between the D$_i^0$X and its TES$_i$ is the difference between the donor energies in the 1s and 2s/2p states. The donor excitation energy from the ground state to the first excited state is equal to three-fourths of the donor binding energy (E_D).[27,29] According to the TES and D^{0}X peak positions, we calculated the E_D as 50.7 meV. The binding energy of a neutral donor exciton was estimated as 15 meV based on the energy difference between the FX and D^{0}X emissions. This value is nearly identical to the activation energy for the thermal release

of excitons from neutral donors. The E_D is estimated as 50 meV based on Haynes' empirical rule.[27]

To study the origin of the UV emission in sample 3, PL spectra were measured at various temperatures from 12 to 300 K, as shown in Figure 7a. The D^{0}X emission was dominant at
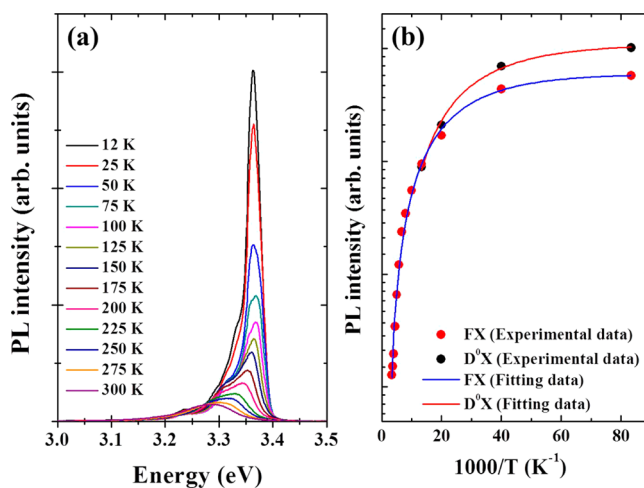

Figure 7. (a) The temperature-dependent PL spectra of sample 3 NBE emission, and (b) the integrated dependence of PL intensity dependence on temperature. The solid line is a fit to experimental data using eq 8.

12 K. However, the FX emission became dominant above 75 K, indicating that it was more probable for the bound excitons to ionize and eventually become FXs as the temperature increased. The intensity of all PL peaks decreased with increasing temperature from 12 to 300 K, resulting from the thermally induced dissociation of electron−hole pairs as described by[30]

$$I = I_0/[1 + C \exp(-\Delta E_A/k_B T)] \tag{8}$$

where I_0 is the emission intensity at T = 0 K, C is a constant, k_B is Boltzmann's constant, and ΔE_A is the activation energy for thermal quenching. The advantage of a large exciton binding energy for some device applications is clearly apparent in eq 8. Indeed, the PL intensity increased nearly exponentially with the activation (binding or localization) energy at a given temperature. Figure 7b shows the PL intensities of the D^{0}X and FX peaks as a function of inverse temperature for sample 3. The curves in Figure 7b represent the best-fit results according to eq 8. The activation energy was 15 meV for the D^{0}X peaks and 61 meV for the FX peaks. These activation energies accurately reflect the properties indicated by the PL spectrum of sample 3 (Figure 6). Namely, the D^{0}X peaks at T < 75 K originate from the recombination of donor-bound excitons with a localization energy of 15 meV, a value identical to the localization energy in Figure 6, while the FX peaks at T > 75 K originate from the recombination of free excitons with a binding energy of ∼61 meV, a value nearly identical to the exciton binding energy of ZnO (60 meV).

To form the electrodes, Al and In metals were deposited onto the p-Si and n-ZnO, respectively. Figure S5 (Supporting Information) presents the $I−V$ characteristics of the three samples, revealing the rectification behavior. The inset of Supporting Information, Figure S4a shows a schematic of the n-ZnO nanorods or ZnO films with the p-Si as a heterojunction. The turn-on voltage of all three samples was estimated at ∼5.9 V. For the n-ZnO/p-Si heterojunctions annealed in open air,

using FTFA or the VC-FTFA method, the currents at 7.2 V were 0.0013, 0.027, and 14.25 mA, respectively. These results indicate that the VC-FTFA method is an essential process for activating the optical and electrical properties of n-ZnO/p-Si heterojunctions.

4. CONCLUSION

In summary, the ZnO nanorods prepared using the VC-FTFA method exhibited significantly enhanced optical properties compared to ZnO films annealed in open air. The regrowth of the ZnO nanorods was due to the chloride-containing metal, in this case, zinc chloride, which generated $ZnCl_2$ vapor. The growth of the ZnO nanorods can be attributed to the vapor–solid mechanism, in which nanorods grow via the oxidation of produced Zn vapor, followed by condensation. The $ZnCl_2$ vapors decomposed between 400–600 °C, and the Zn vapors absorbed on the round nanoparticles with oxygen-containing organic compounds or with oxygen present in the air. The regrowth resulting from the VC-FTFA method is effective in increasing both the NBE emission intensity as well as emission uniformity. The VC-FTFA method is expected to present a possible route for the low-cost fabrication of optoelectronic devices with high external efficiencies.

■ ASSOCIATED CONTENT

Ⓢ Supporting Information

Additional SEM images of ZnO film using zinc acetate dihydrate precursor as solvent, PL spetra of $Mg_{0.25}Zn_{0.75}O$ film and nanorod, and $I–V$ curves of three samples. This material is available free of charge via the Internet at http://pubs.acs.org.

■ AUTHOR INFORMATION

Corresponding Author
*E-mail: jyleem@inje.ac.kr.
Notes
The authors declare no competing financial interest.

■ ACKNOWLEDGMENTS

■ REFERENCES

(1) Tsivion, D.; Schvartzman, M.; Biro, R. P.; Huth, P. V.; Joselevich, E. Guided Growth of Millimeter-Long Horizontal Nanowires with Controlled Orientations. *Science* **2005**, *333*, 1003−1007.

(2) Liu, X.; Zhang, Q.; Xing, G.; Xiong, Q.; Sum, T. C. Size-Dependent Exciton Recombination Dynamics in Single CdS Nanowires beyond the Quantum Confinement Regime. *J. Phys. Chem. C* **2013**, *117*, 10716−10722.

(3) Yin, H.; Wang, Q.; Geburt, S.; Milz, S.; Ruttens, B.; Degutis, G.; D'Haen, J.; Shan, L.; Punniyakoti, S.; D'Olieslaeger, M.; Wagner, P.; Ronning, C.; Boyen, H.-G. Controlled Synthesis of Ultrathin ZnO Nanowires Using Micellar Gold Nanoparticles as a Catalyst Templates. *Nanoscale* **2013**, *5*, 7046−7053.

(4) Li, S.; Zhang, C.; Li, F.; Ji, W.; Li, P.; Ren, M.; Wang, P.; Yuan, M. Prediction of Half-Metallic Ferromagnetism in C-Doped CdS Nanowire. *RSC Adv.* **2014**, *4*, 24399−24405.

(5) Yu, R.; Pan, C.; Chen, J.; Zhu, G.; Wang, Z. L. Enhanced Performance of a ZnO Nanowire-Based Self-Powered Glucose Sensor by Piezotronic Effect. *Adv. Funct. Mater.* **2013**, *23*, 5868−5874.

(6) Mohammad, S. N. Metal/Nanowire Contacts, Quantum Confinement, and Their Roles in the Generation of New. *Nanotechnology* **2013**, *24*, 455201.

(7) Nguyen, H.; Quy, C. T.; Hoa, N. D.; Lam, N. T.; Duy, N. V.; Quang, V. V.; Hieu, N. V. Controllable Growth of ZnO Nanowires Grown on Discrete Islands of Au Catalyst for Realization of Planar-Type Micro Gas Sensor. *Sens. Actuators, B* **2014**, *193*, 888−894.

(8) Qian, F.; Gradecak, S.; Li, Y.; Wen, C.-Y.; Lieber, C. M. Core/Multishell Nanowire Heterostructures as Multicolor, High-Efficiency Light-Emitting Diodes. *Nano Lett.* **2005**, *5*, 2287−2291.

(9) Makhonin, M. N.; Foster, A. P.; Krysa, A. B.; Fry, P. W.; Davies, D. G.; Grange, T.; Walther, T.; Skolnick, M. S.; Wilson, L. R. Homogeneous Array of Nanowire-Embedded Quantum Light Emitters. *Nano Lett.* **2013**, *13*, 861−865.

(10) Huang, M. H. Room-Temperature Ultraviolet Nanowire Nanolasers. *Science* **2001**, *292*, 1897−1899.

(11) Lu, Y.; Dajani, I. A.; Knize, R. J. ZnO Nanorod Arrays as p-n Heterojunction Ultraviolet Photodetectors. *Electron. Lett.* **2006**, *42*, 1309−1310.

(12) Suh, D.-I.; Lee, S.-Y.; Hyung, J.-H.; Kim, T.-H.; Lee, S.-K. Mutiple ZnO Nanowires Field-Effect Transistor. *J. Phys. Chem. C* **2008**, *112*, 1276−1281.

(13) Fan, J.; Hao, Y.; Munuera, C.; Garcia-Hernandez, M.; Guell, F.; Johansson, E. M. J.; Boschloo, G.; Hagfeldt, A.; Cabot, A. Influence of the Annealing Atmosphere on the Performance of ZnO Nanowire Dye-Sensitized Solar Cells. *J. Phys. Chem. C* **2013**, *117*, 16349−16356.

(14) Barreca, D.; Bekermann, D.; Commi, E.; Devi, A.; Fischer, R. A.; Gasparotto, A.; Maccato, C.; Sada, C.; Sberveglieri, G.; Tondello, E. Urchin-Like ZnO Nanorod Arrays for Gas Sensing Applications. *CrystEngComm* **2010**, *12*, 3419−3421.

(15) Guo, P.; Zheng, Y.; Wen, M.; Song, C.; Lin, Y.; Jiang, L. Icephobic/Anti-Icing Properties of Micro/Nanostructured Surfaces. *Adv. Mater.* **2012**, *24*, 2642−2648.

(16) Chen, C.-Y.; Huang, J.-H.; Song, J.; Zhou, Y.; Lin, L.; Zhang, P.-C.; Liu, C.-P.; He, J.-H.; Wang, Z. L. Anisotropic Outputs of a Nanogenerator from Oblique-Aligned ZnO Nanowire Arrays. *ACS Nano* **2011**, *5*, 6707−6713.

(17) Shi, Z.-F.; Zhang, Y.-T.; Cai, X.-P.; Wang, H.; Wu, B.; Zhang, J.-X.; Cui, X.-J.; Dong, X.; Liang, H.-W.; Zhang, B.-L.; Du, G.-T. Parametric Study on the Controllable Growth of ZnO Nanostrucutures with Tunable Dimensions Using Catalyst-Free Metal Organic Chemical Vapor Deposition. *CrystEngComm* **2014**, *16*, 455−463.

(18) Zhu, R.; Zhang, W.; Li, C.; Yang, R. Uniform Zinc Oxide Nanowire Arrays Grown on Nonepitaxial Surface with General Orientation Control. *Nano Lett.* **2013**, *13*, 5171−5176.

(19) Hou, J.-L.; Chang, S.-J.; Hsueh, T.-J.; Wu, C.-H.; Weng, W.-Y.; Shieh, J.-M. InGaP/GaAs/Ge Triple-Junction Solar Cells with ZnO Nanowires. *Prog. Photovoltaics* **2013**, *21*, 1645−1652.

(20) Shinaqawa, T.; Izaki, M. Morphological Evolution of ZnO Nanorod Arrays Induced by a pH-Buffering Effect during Electrochemical Deposition. *RSC Adv.* **2014**, *4*, 30999−31002.

(21) Pu, X.; Liu, J.; Liang, J.; Yusheng, X.; Feng, W.; Wang, Y.; Yu, X. Effective CdS/ZnO Nanorod Arrays as Antireflection Coating for Light Trapping in c-Si Solar Cells. *RSC Adv.* **2014**, *4*, 23149−23154.

(22) Kanber, H.; Cipolli, R. J.; Henderson, W. B.; Whelan, J. M. A Comparison of Rapid Thermal Annealing and Controlled Atmosphere Annealing of Si-Implanted GaAs. *J. Appl. Phys.* **1985**, *57*, 4732−4737.

(23) Paraguay D, F.; Estrada L, W.; Acosta N, D. R.; Andrade, E.; Miki-Yoshida, M. Growth, Structure and Optical Characterization of High Quality ZnO Thin Films Obtained by Spray Pyrolysis. *Thin Solid Films* **1999**, *350*, 192−202.

(24) Lin, C.-C.; Li, Y.-Y. Synthesis of ZnO Nanowires by Thermal Decomposition of Zinc Acetate Dihydrate. *Mater. Chem. Phys.* **2009**, *113*, 334−337.

(25) Vanheusden, K.; Seager, C. H.; Warren, W. L.; Tallant, D. R.; Voigt, J. A. Correlation between Photoluminescence and Oxygen Vacancies in ZnO Phosphors. *Appl. Phys. Lett.* **1996**, *68*, 403−405.

(26) Wang, Y. G.; Lau, S. P.; Zhang, W. H.; Hng, H. H.; Lee, H. W.; Yu, S. G.; Tay, B. K. Enhancement of Near-Band-Edge Photoluminescence from ZnO Films by Face-to-Face Annealing. *J. Cryst. Growth* **2003**, *259*, 335−342.

(27) Özgür, Ü.; Alivov, Ya. I.; Liu, C.; Teke, A.; Reshchikov, M. A.; Doğan, S.; Avrutin, V.; Cho, S.-J; Morkoc, H. A Comprehensive Review of ZnO Materials and Devices. *J. Appl. Phys.* **2005**, *98*, 041301.

(28) Johnston, K.; Henry, M. O.; McCabe, D.; McGlynn, E.; Dietrich, M.; Alves, E.; Xia, M. Identification of Donor-Related Impurities in ZnO Using Photoluminescence and Radiotracer Techniques. *Phys. Rev. B* **2006**, *73*, 165212.

(29) Chiu, H.-M.; Chang, Y.-T.; Wu, W.-W.; Wu, J.-M. Synthesis and Characterization of One-Dimensional Ag-Doped ZnO/Ga-Doped ZnO Coaxial Nanostructure Diodes. *ACS Appl. Mater. Interfaces* **2014**, *6*, 5183−5191.

(30) Schuster, F.; Laumer, B.; Zamani, R. R.; Mağen, C.; Morante, J. R.; Arbiol, J.; Stutzmann, M. p-GaN/n-ZnO Heterojunction Nanowires: Optoelectronic Properties and the Role of Interface Polarity. *ACS Nano* **2014**, *8*, 4376−4384.